Geophysical Prospecting

EAGE EUROPEAN ASSOCIATION OF GEOSCIENTISTS & ENGINEERS

Geophysical Prospecting, 2017 doi: 10.1111/1365-2478.12488

Parsimonious wave-equation travel-time inversion for refraction waves

Lei Fu[1]*, Sherif M. Hanafy[1,2] and Gerard T. Schuster[1]

[1]*Physical Science and Engineering Division, King Abdullah University of Science and Technology, Thuwal 23955, Saudia Arabia, and* [2]*Geophysics Department, Cairo University, Giza 12613, Egypt*

Received June 2016, revision accepted November 2016

ABSTRACT

We present a parsimonious wave-equation travel-time inversion technique for refraction waves. A dense virtual refraction dataset can be generated from just two reciprocal shot gathers for the sources at the endpoints of the survey line, with N geophones evenly deployed along the line. These two reciprocal shots contain approximately $2N$ refraction travel times, which can be spawned into $O(N^2)$ refraction travel times by an interferometric transformation. Then, these virtual refraction travel times are used with a source wavelet to create N virtual refraction shot gathers, which are the input data for wave-equation travel-time inversion. Numerical results show that the parsimonious wave-equation travel-time tomogram has about the same accuracy as the tomogram computed by standard wave-equation travel-time inversion. The most significant benefit is that a reciprocal survey is far less time consuming than the standard refraction survey where a source is excited at each geophone location.

Key words: Refraction tomography, WT, Acquisition.

INTRODUCTION

Inversion of refraction-wave traveltimes is often used to estimate the Earth's velocity model in earthquake studies (Stein and Wysession 2009), crustal-mantle imaging (White and Clowes 1990; Korenaga *et al.* 2000; Prodehl and Mooney 2012), seismic exploration (Hole 1992), and engineering seismology (Lanz, Maurer and Green 1998; Zhang and Toksoz 1998). Typically, a dense distribution of geophones is deployed along the survey line, and common shot gathers are recorded for different source locations. To minimise the data acquisition time, a parsimonious survey is proposed by Hanafy and Schuster (2016) so that the sources are only located at each end of the survey line. Then, virtual shot gathers with virtual sources located at each geophone position can be generated from these two reciprocal shot gathers by parsimonious refraction interferometry. It is a special use of Fermat's interferometric travel-time principle (Schuster 2005) and closure phase (Schuster *et al.* 2014) that allows for the decomposition of long raypaths and travel times into shorter raypaths and travel times, respectively. The underlying assumption is that the refraction arrivals are head waves. Hanafy and Schuster (2016) tested parsimonious tomography with a ray-tracing travel-time inversion (RT) method. In this paper, we now test it with the wave-equation travel-time inversion (WT) method (Luo and Schuster 1991), which updates the velocity by smearing the travel-time residuals along wavepaths, not raypaths.

The next section describes the theory of parsimonious refraction interferometry and the WT method. Section 3 presents the numerical results for applying parsimonious WT to both synthetic and field data; we also compare WT to RT for virtual data generated by parsimonious refraction interferometry. The final section presents the summary and discussion.

THEORY

Assume two reciprocal sources and the irregularly layered medium in Fig. 1, where head waves propagate along the interface between the upper and lower layers. There can be lateral velocity variations in the upper medium, and there are N evenly spaced geophones on the recording surface between

*E-mail: lei.fu@kaust.edu.sa

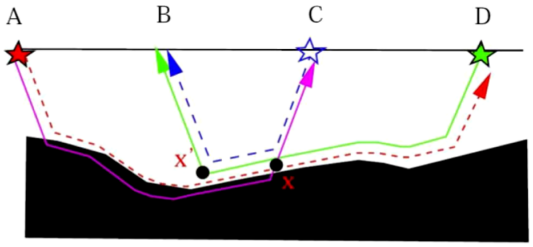

Figure 1 Two-layer model where the black medium is faster than the top layer; the reciprocal sources are at **A** and **D** and the corresponding refraction raypath is denoted by the dashed red ray. The dashed blue raypath is associated with the virtual refraction ray that is excited by the virtual source (blue star) at **C** and terminates at **B**. The refraction travel times associated with the reciprocal shots (green and red stars) can be decomposed into the virtual refraction travel time generated by the blue star (see equation 3 and Fig. 10 in Schuster *et al.* (2014)).

the two sources. The head-wave travel time from the source at **A** to the geophone at **C** is defined as

$$\tau_{AC} = \tau_{Ax'} + \tau_{x'x} + \tau_{xC}, \tag{1}$$

and the reciprocal travel time from **D** to **B** is

$$\tau_{DB} = \tau_{Dx} + \tau_{x'x} + \tau_{xB}, \tag{2}$$

where $\tau_{xx'}$ is the travel time from $\mathbf{x}$ to $\mathbf{x}'$ along the refraction ray, and reciprocity states that $\tau_{xx'} = \tau_{x'x}$. Travel times τ_{AC} and τ_{DB} are denoted as a pair of reciprocal travel times.

Virtual refraction dataset

To create virtual sources and receivers within the array in Fig. 1, we assume that there is a postcritical distance between the geophone positions **C** and **B**. Subtracting the reciprocal travel time $\tau_{AD} = \tau_{Ax'} + \tau_{x'x} + \tau_{xD}$ from the sum $\tau_{AC} + \tau_{DB}$ gives the following virtual travel time $\delta\tau_{CB}$:

$$\begin{aligned}\delta\tau_{CB} &= \tau_{AC} + \tau_{DB} - \tau_{AD} \\ &= \tau_{Ax'} + \tau_{x'x} + \tau_{xC} + [\tau_{Dx} + \tau_{xx'} + \tau_{x'B}] \\ &\quad - [\tau_{Ax'} + \tau_{x'x} + \tau_{xD}] \\ &= \tau_{Cx} + \tau_{xx'} + \tau_{x'B}.\end{aligned} \tag{3}$$

Equation (3) can be used to generate $O(N^2)$ head-wave travel times in N virtual shot gathers (Schuster *et al.* 2014), where the number of reciprocal geophone pairs with postcritical separation is assumed to be nearly equal to the number N of geophones in the survey. The virtual refraction travel times are used to time shift an extracted wavelet to obtain virtual refraction traces, which can then be used to invert for the subsurface velocity model with wave-equation travel-time inversion.

Wave-equation travel-time inversion

For seismic data, refraction waves can be modelled by solving the 2D constant-density acoustic wave equation as follows:

$$\nabla p^2(\mathbf{x}, t) - \frac{1}{v(\mathbf{x})^2}\frac{\partial^2 p(\mathbf{x}, t)}{\partial t^2} = f(\mathbf{x}, t), \tag{4}$$

where $v(\mathbf{x})$ is the P-wave velocity model, $p(\mathbf{x}, t)$ is the pressure field, and $f(\mathbf{x}, t)$ is the source term.

The WT method is designed to find the velocity model that minimizes the following objective function:

$$\Phi(\mathbf{v}) = \frac{1}{2}\|\Delta\tau_{rs}\|^2, \tag{5}$$

where $\Delta\tau_{rs} = \tau_{cal}(\mathbf{x}_r, \mathbf{x}_s) - \tau_{obs}(\mathbf{x}_r, \mathbf{x}_s)$ is the refraction travel-time residual for a source at $\mathbf{x}_s$ and a receiver at $\mathbf{x}_r$ (Luo and Schuster 1991). In practice, the travel-time difference can be found by cross-correlating the predicted and the observed seismograms. The P-velocity distribution can be iteratively updated using any gradient-based method such as the conjugate gradient method

$$\mathbf{v}_{k+1} = \mathbf{v}_k + \alpha_k \mathbf{d}_k, \tag{6}$$

where $\mathbf{v}_k$ is the P-velocity model at the k^{th} iteration; α_k is the step length, which can be found by a line search algorithm

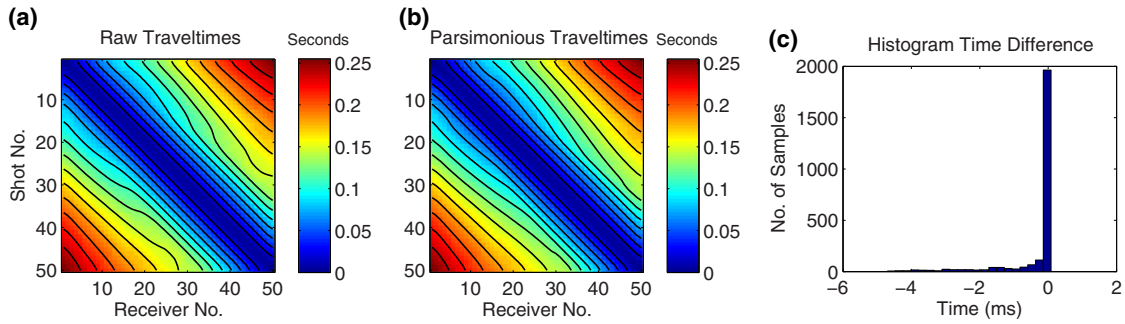

Figure 2 (a) Raw first-arrival travel times. (b) Virtual travel times for the two-layer simple model. (c) Time-difference histogram for (a) and (b).

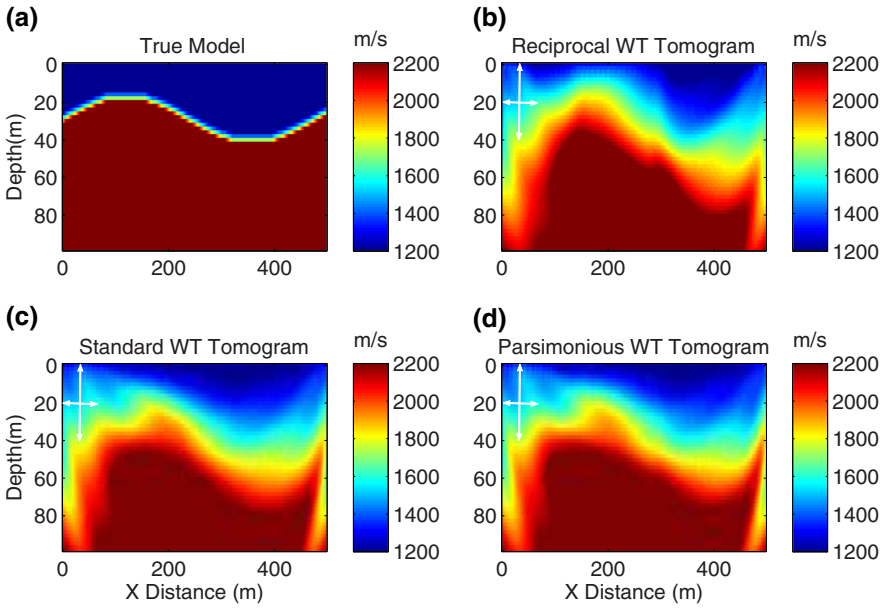

Figure 3 (a) True two-layer model. (b) Reciprocal WT tomogram inverted from two reciprocal shot gathers. (c) Standard WT tomogram inverted from 50 raw shot gathers. (d) Parsimonious WT tomogram inverted from 50 virtual shot gathers generated from two reciprocal shot gathers. The dominant wavelength of the source is indicated by the double-sided arrow.

(Byrd, Nocedal and Schnabel 1994); and $\mathbf{d}_k$ is the update direction

$$\mathbf{d}_k = -\mathbf{g}_k + \beta_k^p \mathbf{d}_{k-1}, \tag{7}$$

$$\beta_k = \frac{(\mathbf{g}_k - \mathbf{g}_{k-1}, \mathbf{g}_k)}{(\mathbf{g}_{k-1}, \mathbf{g}_{k-1})}. \tag{8}$$

The current search direction $\mathbf{d}_k$ employs derivatives of the misfit function with respect to the current model parameter, e.g., $\mathbf{g}_k = \frac{\partial \Phi}{\partial \mathbf{v}_k}$, and the former search direction $\mathbf{d}_k$. Since the WT is a non-linear inversion method, we use a line search method to get the step length.

In WT, the gradient of the misfit function with respect to the P-wave velocity is given by (Luo and Schuster 1991)

$$\mathbf{g} = \frac{1}{\mathrm{v}^3} \sum_s \int \dot{p}(\mathbf{x}, t|\mathbf{x}_s)_{cal}\, \dot{p}'(\mathbf{x}, t|\mathbf{x}_r) dt, \tag{9}$$

where

$$\dot{p}'(\mathbf{x}, t|\mathbf{x}_s) = \sum_r G(\mathbf{x}, -t|\mathbf{x}_r, 0) * \delta\tau(\mathbf{x}_r, t|\mathbf{x}_s), \tag{10}$$

and the symbol $*$ represents temporal convolution, $\dot{p}$ represents the time derivative of p, and $G(\mathbf{x}, -t|\mathbf{x}_r, 0)$ is the Green's function associated with equation (1) for the velocity field v^p. $p'(\mathbf{x}, t|\mathbf{x}_s)$ is the pressure field computed by back propagating the pseudo-residual $\delta\tau(\mathbf{x}_r, t|\mathbf{x}_s)$ in reverse time. The pseudo-residual is obtained by weighting the time-shifted observed seismogram at receiver $\mathbf{x}_r$ with its associated travel-time residual $\Delta\tau_{rs}$ as follows:

$$\delta\tau(\mathbf{x}_r, t|\mathbf{x}_s) = -\frac{2}{E}\, \dot{p}(\mathbf{x}_r, t + \Delta\tau_{rs}|\mathbf{x}_s)_{obs}\, \Delta\tau_{rs}, \tag{11}$$

where the normalisation factor E is defined as

$$E = \int \dot{p}(\mathbf{x}_r, t + \Delta\tau_{rs}|\mathbf{x}_s)_{obs}\, \dot{p}(\mathbf{x}_r, t|\mathbf{x}_s)_{cal}\, dt. \tag{12}$$

The WT method is used to iteratively find the velocity model that minimises the misfit function in equation (5) until the

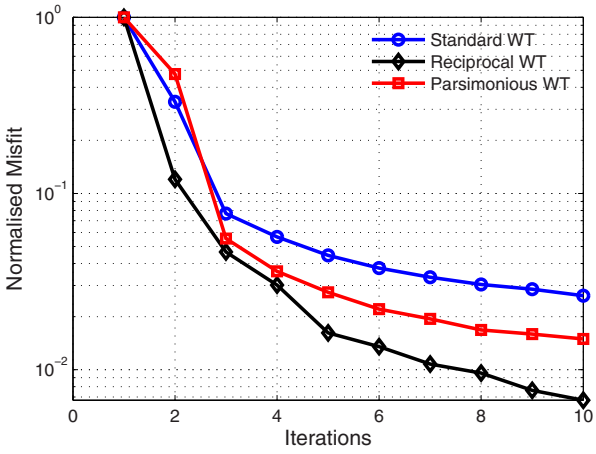

Figure 4 Normalised misfit plotted against iteration numbers.

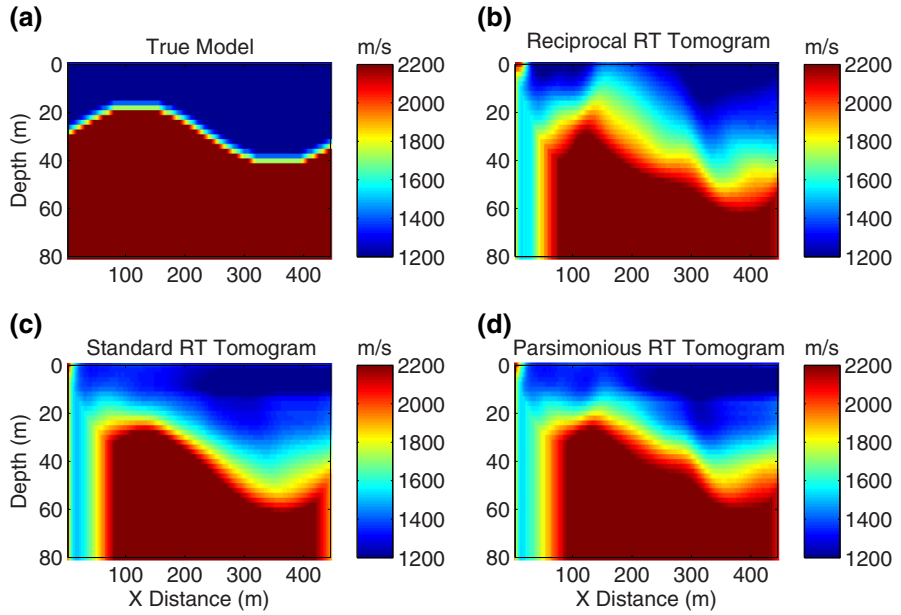

Figure 5 (a) True two-layer model. (b) Reciprocal RT tomogram inverted from the travel times of two reciprocal shot gathers. (c) Standard RT tomogram inverted from the travel times of 50 raw shot gathers. (d) Parsimonious RT tomogram inverted from the traveltimes of 50 virtual shot gathers generated from two reciprocal shot gathers.

standard deviation of the residual falls below the estimated picking error.

NUMERICAL RESULTS

Parsimonious wave-equation travel-time inversion (WT) for refraction waves will be tested on two synthetic models and one field dataset.

Two-layer simple model

The refraction traveltimes and the two-layer simple model are shown in Figs. 2 and 3, respectively. The velocity in the top layer is 1200 m/s, and the velocity in the bottom layer is 2200 m/s. The model is discretised into 50 × 250 gridpoints with a gridpoint interval of 2 m. A finite-difference solution to the acoustic wave equation is used to obtain 50 shot gathers with 50 geophones evenly deployed on the surface with 10-m intervals. The source wavelet is a Ricker wavelet with a peak frequency of 30 Hz.

The raw first-arrival travel times shown in Fig. 2a are picked from the 50 synthetic shot gathers. These raw first-arrival travel times are convolved with a 30-Hz Ricker wavelet to obtain 50 raw shot gathers, which are the input data for the standard WT. The standard WT tomogram after ten iterations is shown in Fig. 3c, which mostly agrees with the true model.

The two reciprocal shot gathers only contain 100 first-arrival travel times, where one shot is at (0, 0) m and the other is located at (500, 0) m. These 100 first-arrival travel times are used to time shift a Ricker wavelet with a peak frequency of 30 Hz to obtain two reciprocal shot gathers, and the corresponding reciprocal WT tomogram is shown in Fig. 3b. In this example, the reciprocal WT tomogram largely agrees with the true model, but this is not surprising because the velocity model is simple.

Equation (3) is then used to generate the parsimonious travel times from the 100 first-arrival travel times associated with the two reciprocal shot gathers. The parsimonious travel times are plotted in Fig. 2b, and the time-difference histogram associated with the raw and parsimonious travel times is shown in Fig. 2c. The plots show that most of the travel times

Table 1 RMS velocity errors for different tomograms associated with the two-layer simple model.

	Reciprocal	Standard	Parsimonious
WT	10.79%	10.71%	10.73%
RT	14.23%	13.85%	13.46%

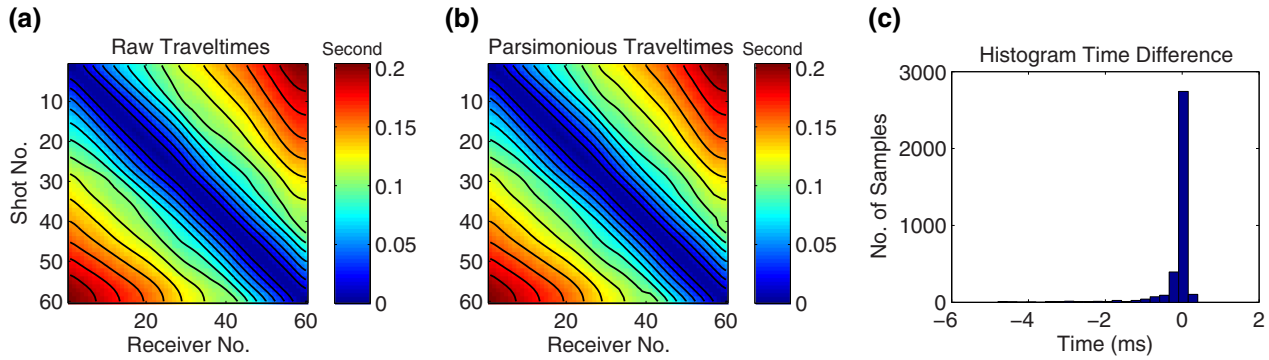

Figure 6 (a) Raw first-arrival travel times. (b) Virtual travel times. (c) Time-difference histogram for (a) and (b).

from parsimonious refraction interferometry agree well with the observed travel times. Also, we can find that the time differences are less than 7 ms, which is less than a quarter of the dominant period $\frac{1}{4}T$. Then, the parsimonious traces in the shot gathers are obtained by time-shifting Ricker wavelets by the virtual travel times computed from equation (3). Inverting these virtual traces by the WT method gives the corresponding parsimonious WT tomogram shown in Fig. 3d, which is almost the same as the standard WT tomogram.

Figure 4 shows the normalised misfit values for standard WT, reciprocal WT, and parsimonious WT. The reciprocal WT has the fastest convergence rate because it has many fewer travel times to predict compared with standard WT and parsimonious WT.

For the comparison of WT with ray-based tomography, we apply RT to the first-arrival travel times associated with the synthetic model shown in Fig. 2, and the resulting reciprocal, parsimonious, and standard tomograms are shown in Fig. 5. In this case, the RT tomograms largely agree with those computed from the WT methods.

The root-mean-square (RMS) velocity error is defined as $\epsilon = \sqrt{\sum(\Delta v)^2}/\sqrt{\sum v_{true}^2}$, where the summation is over all the pixels in the velocity model and Δv is the velocity difference between the inverted velocity tomogram and the true velocity

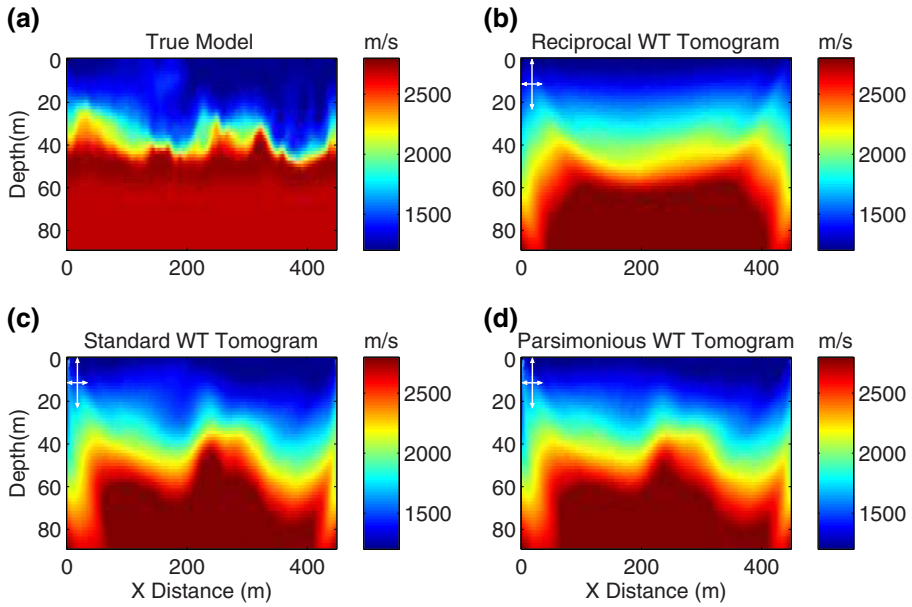

Figure 7 (a) True complex model. (b) Reciprocal WT tomogram inverted from the two reciprocal shot gathers. (c) Standard WT tomogram inverted from the 60 raw shot gathers. (d) Parsimonious WT tomogram inverted from the 60 virtual shot gathers generated from two reciprocal shot gathers. The dominant wavelength of the source is indicated by the double-sided white arrow.

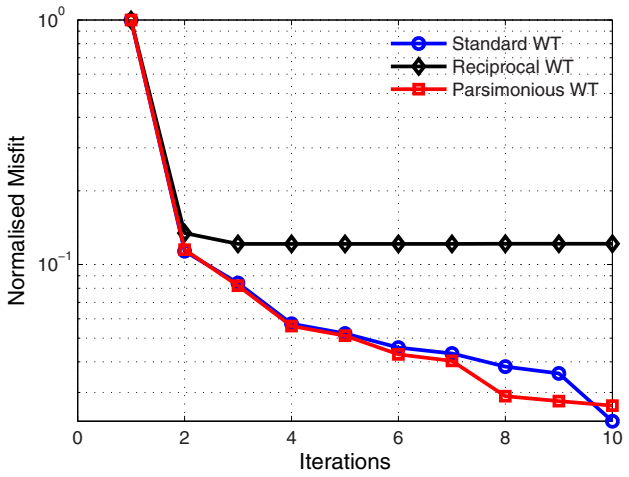

Figure 8 Normalised misfit values plotted against iteration numbers.

model v_{true} in a specified pixel. Here, the summation is over all of the pixels in the model. Table 1 shows the RMS velocity errors for both the WT and RT tomograms. We can see that the RMS velocity errors for parsimonious inversion are very close to those obtained by standard inversion. The RMS velocity errors of reciprocal inversion are slightly larger than those of the other two inversions. Also, we can find that the RMS velocity errors for the WT method are less than those for the RT method.

Table 2 RMS velocity errors for different tomograms associated with the complex model.

	Reciprocal	Standard	Parsimonious
WT	12.83%	11.59%	11.53%
RT	18.38%	15.73%	15.18%

Complex model

The refraction traveltimes and the associated complex velocity model are shown in Figs. 6 and 7, respectively. In Fig. 7a, the velocity model is discretised into 60 × 300 gridpoints with the grid size of 1.5 m. A finite-difference solution to the 2D acoustic wave equation is used to compute 60 shot gathers with 60 geophones evenly deployed on the surface with a 7.5-m interval. The source wavelet is a Ricker wavelet with a peak frequency of 50 Hz.

The raw first-arrival travel times represented in Fig. 6a are extracted from the 60 synthetic shot gathers. These travel times are used to time shift a 50-Hz Ricker wavelet to generate 60 raw shot gathers, which are the input data for standard WT. The standard WT tomogram is shown in Fig. 7c, which is in good agreement with a smoothed version of the true model.

The first-arrival travel times can be picked from the two reciprocal shot gathers to give 120 first-arrival travel times,

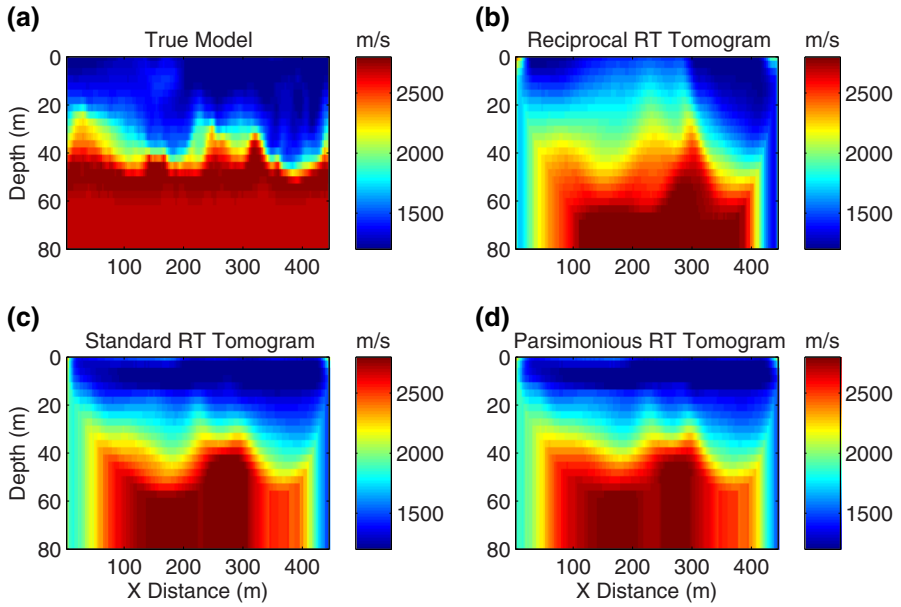

Figure 9 (a) True complex velocity model. (b) Reciprocal RT tomogram inverted from the travel times of two reciprocal shot gathers. (c) Standard RT tomogram inverted from the travel times of 60 raw shot gathers. (d) Parsimonious RT tomogram inverted from the travel times of 60 virtual shot gathers generated from two reciprocal shot gathers.

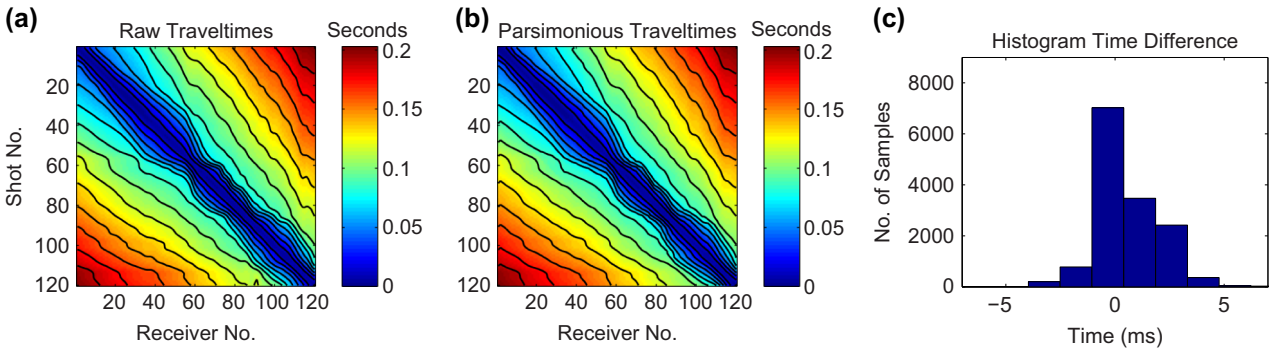

Figure 10 (a) Raw first-arrival travel times extracted from the observed 120 shot gathers. (b) Virtual travel times. (c) Time-difference histogram for (a) and (b).

where one shot is at (0, 0) m and the other is located at (450, 0) m. These 120 first-arrival travel times are used to time shift a 50-Hz Ricker wavelet to obtain two reciprocal shot gathers, and the corresponding reciprocal WT tomogram is shown in Fig. 7b. It shows that the reciprocal WT tomogram is far from the true model.

Equation (3) is then used to generate the parsimonious travel times from the 120 first-arrival travel times associated with the two reciprocal shot gathers. The parsimonious travel times are shown in Fig. 6b, and the time-difference histogram between the raw and parsimonious travel times is shown in Fig. 6c. The results show that most of the travel times from parsimonious refraction interferometry agree well with the observed travel times. Also, we can find that the time differences are less than 5 ms, which is less than a quarter of the dominant period $\frac{1}{4}T$. The corresponding parsimonious WT tomogram is shown in Fig. 6d, which is almost the same as the standard WT tomogram.

Figure 8 shows the normalised misfit values for the standard WT, reciprocal WT and parsimonious WT methods plotted against iteration number. For reciprocal WT, the inversion gets stuck at a local minimum. However, parsimonious WT has a nearly identical convergence rate compared with the standard WT.

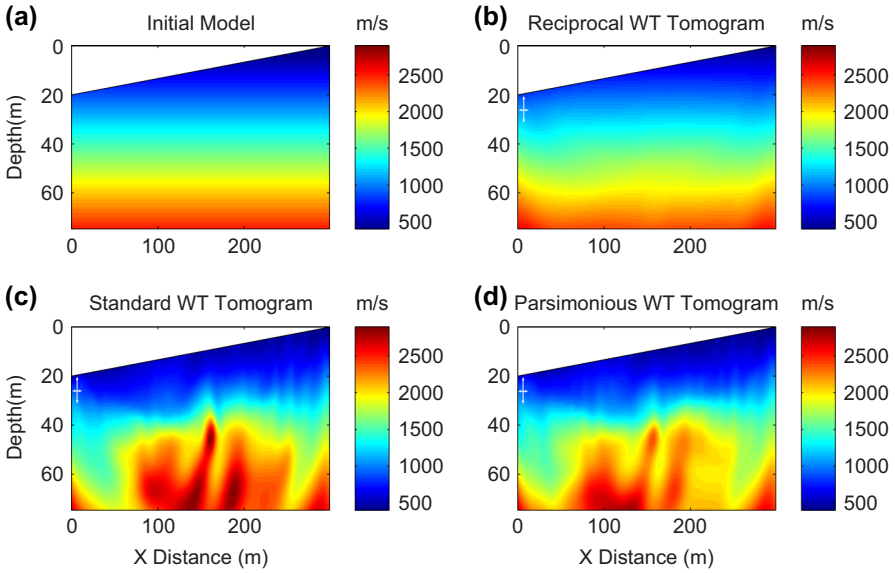

Figure 11 (a) Initial velocity model. (b) Reciprocal WT tomogram inverted from the travel times of two reciprocal shot gathers. (c) Standard WT tomogram inverted from the travel times of 120 raw shot gathers. (d) Parsimonious WT tomogram inverted from the travel times of 120 virtual shot gathers generated from two reciprocal shot gathers. The dominant wavelength of the source is indicated by the double-sided white arrow.

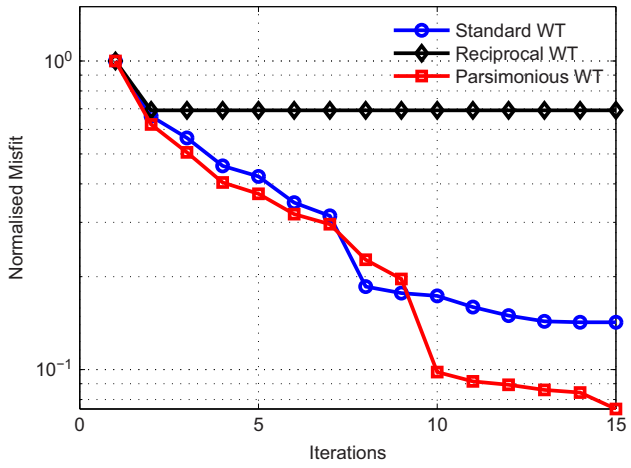

Figure 12 Normalised misfit values plotted against iteration numbers.

For the comparison of WT with RT, we apply RT to travel times associated with the synthetic model shown in Fig. 7a, and the resulting reciprocal, parsimonious, and standard tomograms are shown in Fig. 9. We can see that the standard and parsimonious RT tomograms represent a smoothed approximation of the true model, whereas the reciprocal RT tomogram is a worse approximation to the true model.

Table 2 shows the RMS velocity errors for both the WT and RT tomograms. We can see that the RMS velocity errors for parsimonious inversion are very close to those from the standard inversion. The RMS velocity errors of reciprocal inversion are larger than those of the other two inversions. Also, the RMS velocity errors for the WT method are less than those for the RT method.

Aqaba field data example

Along the western coast of Saudia Arabia, an earthquake rupture located near the Gulf of Aqaba can be seen at the surface (Klinger *et al.* 1999). In order to investigate the geometry of the fault and the alluvial sediments across the fault, a seismic survey was carried out near the Gulf of Aqaba in November 2013. The first-arrival travel times, velocity models, misfit values, and pictures from the survey site are shown in Figs. 10, 11, 12, and 13 respectively. Figures 13a and 13b show the fault rupture due to the 1995 earthquake (Klinger *et al.* 1999). The black arrow in Fig. 13a indicates the location of the resistivity and seismic survey lines, which are perpendicular to the fault.

The resistivity profile consists of 64 electrodes with a spacing interval of 5 m; the Schlumberger–Wenner configuration array was used to acquire the resistivity data. The resistivity tomogram was inverted from the Res2DInv software to give the result in Fig. 13c. We can find two layers in the resistivity tomogram. The resistivity values of the top layer range from 400 to 500 Ω-m on the left side and from 250 to 400 Ω-m on the right side. The thickness of the top layer ranges from 6 to 10 m. The bottom layer has low resistivity values ranging from 10 to 50 Ω-m. However, the fault

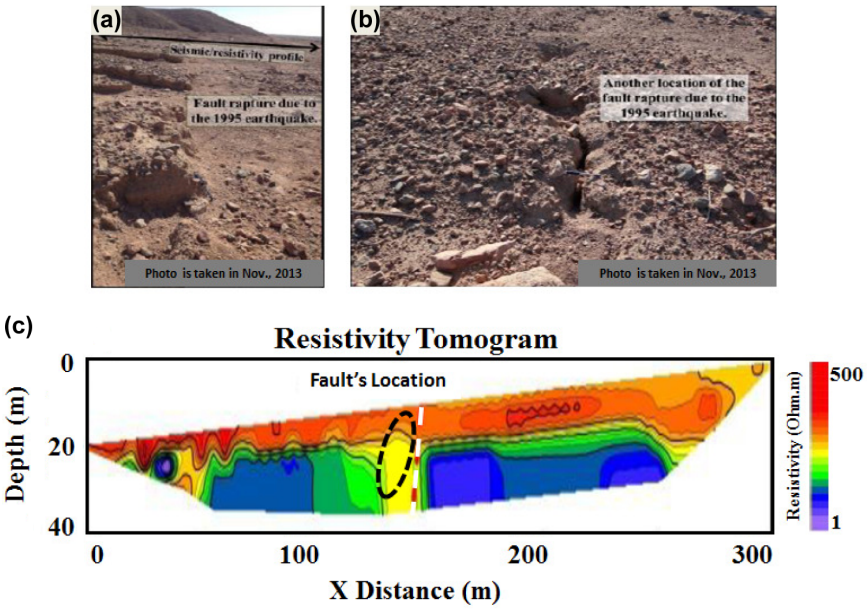

Figure 13 (a) Photo showing the seismic profile perpendicularity across the fault. (b) Photo showing the fault rupture due to the 1995 earthquake. (c) The resistivity tomogram, where the white-dashed line shows the suggested fault location extrapolated from the fault's location at the surface.

location is shown as a vertical anomaly indicated by the black dashed ellipse between 130 m and 150 m along the horizontal axis.

The seismic data consist of traces recorded by 120 vertical-component geophones deployed at 2.5-m intervals along the survey line. A 90-kg accelerated weight drop was used for the source at every geophone position to record 120 common shot gathers. The initial velocity model for WT is a gradient velocity model similar to that shown in Fig. 11a, which is discretised into 150×598 gridpoints with the grid size of 0.5 m.

The raw first-arrival travel times represented in Fig. 10a are extracted from the 120 observed shot gathers. These first-arrival travel times are used to time shift a 60-Hz Ricker wavelet to obtain 120 shot gathers, which are the input data for standard WT inversion. The standard WT tomogram is shown in Fig. 11c. We can find a sharp horizontal velocity gradient from 140 to 150 m along the horizontal axis, which is consistent with the resistivity tomogram.

The two reciprocal shot gathers contain 240 first-arrival travel times, where one shot is at (0, 20) m and the other is located at (300, 0) m. These 240 first-arrival travel times are used to time shift a 60-Hz Ricker wavelet to obtain two reciprocal shot gathers, and the corresponding reciprocal WT tomogram is shown in Fig. 11b very different than the WT tomograms.

The parsimonious travel times are shown in Fig. 10b, where the time-difference histogram is shown in Fig. 10c. The statistics show that most of the travel times from parsimonious refraction interferometry agree well with the observed travel times. In addition, the time differences are less than 5 ms, which is less than a quarter of the dominant period $\frac{1}{4}T$. The corresponding parsimonious WT tomogram is shown in Fig. 11d, which is almost the same as the standard WT tomogram.

Figure 12 shows the normalised misfit values for standard WT, reciprocal WT, and parsimonious WT plotted against iteration number. The parsimonious WT has a convergence rate that is nearly identical to that of standard WT. As for the reciprocal WT, it has the worse convergence rate compared with standard WT.

DISCUSSION AND SUMMARY

We present the results of applying parsimonious wave-equation travel-time inversion to refraction travel times. Numerical results on synthetic examples show reciprocal WT or RT will yield tomograms with sub-optimal accuracy.

In contrast, parsimonious interferometry can generate a dense set of virtual refraction travel times from only two reciprocal shot gathers of travel times. The parsimonious WT method can provide nearly the same results as the standard WT method for both simple and complex models. Results from field data suggest that parsimonious WT can provide nearly the same results as the standard WT method.

The root-mean-square velocity errors from the WT tomogram are smaller than those from the RT tomogram for the models we tested. The theoretical benefit of WT is that, unlike RT, it does not require a high-frequency assumption about the data. Moreover, travel times from body waves, diffractions, reflections, and head-wave travel times can be readily incorporated into WT inversion. Therefore, the WT tomogram should provide a more accurate rendering of the subsurface velocity model than RT.

The most significant benefit of the parsimonious WT method is that a reciprocal survey is much less time consuming than the standard refraction survey with a source shooting at each geophone location. The liability, however, is that the travel times are assumed to be those associated with head waves. This means that travel times associated with strong velocity gradients are not suitable for parsimonious interferometry. Such forbidden models can be identified by assessing the flatness of events in common pair offset gathers (Dong *et al.* 2006; Hanafy and Schuster, 2016).

ACKNOWLEDGEMENTS

The research reported in this publication was supported by King Abdullah University of Science and Technology (KAUST) in Thuwal, Saudi Arabia. The authors would like to thank the sponsors of the Center for Subsurface Imaging and Modeling (CSIM) Consortium for their financial support. For computer time, this research used the resources of the Supercomputing Laboratory at KAUST and the IT Research Computing Group. The authors would like to thank them for providing the computational resources required for carrying out this work.

REFERENCES

Byrd R.H., Nocedal J. and Schnabel R.B. 1994. Representations of quasi-Newton matrices and their use in limited memory methods. *Mathematical Programming* **63**, 129–156.

Dong S., Sheng J. and Schuster G.T. 2006. Theory and practice of refraction interferometry. *76th SEG Technical Program Expanded Abstracts*, 3021–3025.

Hanafy S. and Schuster G. 2016. Parsimonious refraction interferometry. *86th SEG Technical Program Expanded Abstracts*, 2339–2343.

Hole J. 1992. Nonlinear high-resolution three-dimensional seismic travel time tomography. *Journal of Geophysical Research: Solid Earth* **97**, 6553–6562.

Klinger Y., Rivera L., Haessler H. and Maurin J.-C. 1999. Active faulting in the Gulf of Aqaba: new knowledge from the Mw 7.3 earthquake of 22 November 1995. *Bulletin of the Seismological Society of America* **89**, 1025–1036.

Korenaga J., Holbrook W., Kent G., Kelemen P., Detrick R., Larsen H.-C. *et al.* 2000. Crustal structure of the southeast Greenland margin from joint refraction and reflection seismic tomography. *Journal of Geophysical Research: Solid Earth* **105**, 21591–21614.

Lanz E., Maurer H. and Green A.G. 1998. Refraction tomography over a buried waste disposal site. *Geophysics* **63**, 1414–1433.

Luo Y. and Schuster G.T. 1991. Wave-equation traveltime inversion. *Geophysics* **56**, 645–653.

Prodehl C. and Mooney W.D. 2012. *Exploring the Earth's Crust: History and Results of Controlled-Source Seismology*, Vol. 208. Geological Society of America.

Schuster G., Huang Y., Hanafy S.M., Zhou M., Yu J. and Alhagan O. 2014. Review on improved seismic imaging with closure phase. *Geophysics* **79**, W11–W25.

Schuster G.T. 2005. Fermat's interferometric principle for target-oriented traveltime tomography. *Geophysics* **70**, U47–U50.

Stein S. and Wysession M. 2009. *An Introduction to Seismology, Earthquakes, and Earth Structure*. John Wiley & Sons.

White D.J. and Clowes R. 1990. Shallow crustal structure beneath the Juan de Fuca Ridge from 2-D seismic refraction tomography. *Geophysical Journal International* **100**, 349–367.

Zhang J. and Toksoz M.N. 1998. Nonlinear refraction traveltime tomography. *Geophysics* **63**, 1726–1737.